Spalling rate of concretes subject to combined leaching and external sulfate attack

Bo Ran, Kefei Li, Teddy Fen-Chong, Othman Omikrine Metalssi, Patrick Dangla

Spalling rate of concretes subject to combined leaching and external sulfate attack

Bo RAN[a,b], Kefei LI[a,*], Teddy FEN-CHONG[b], Othman OMIKRINE-METALSSI[b] and Patrick DANGLA[c]

[a] *Civil Engineering Department, Tsinghua University, Beijing, 100084, China*
[b] *Cerema, UMR MCD, Université Gustave Eiffel, Marne-la-Vallée, F-77454, France*
[c] *Navier, Ecole des Ponts, Université Gustave Eiffel, CNRS, Marne-la-Vallée, F-77447, France*

ARTICLE INFO

Keywords:
Concrete
Durability
Spalling rate
External sulfate attack
Leaching

ABSTRACT

A spalling rate model is established to estimate the damage of concretes subject to the combined action of leaching and external sulfate attack (ESA). Two sub-models are developed to consider the different damage patterns. The profiles of sulfate and hydroxide ions are obtained from the solution of a dual moving boundary problem (MBP). The supersaturation of ettringite crystal is evaluated from these profiles, the effective stress is calculated through poromechanics for pore crystallization, and the spalling depth is determined using the fracture criterion. The experimental validation confirms the proportionality between the spalling depth and the square root of exposure time, and the models give conservative results but on the correct magnitude order for spalling depth. The parametric analysis shows the foremost impact of aluminate content and sulfate diffusivity on damage rate. The main assumptions in models lead to conservative predictions, but yet the model results are meaningful for engineering use.

1. Introduction

The research on concrete materials subject to the external sulfate attack (ESA) has a lengthy history. The first report of sulfate attack dated back to 1818, and the expansive product was identified as ettringite in 1892[1]. Though there are still some debates today, such as the role of gypsum in material expansion[2, 3] and the physical origin of pore pressure creation[4], the general reaction-expansion mechanism of ESA has been rather clarified: the penetration of sulfate ions from external environments disturbs the pore aqueous equilibrium, resulting in the formation of gypsum and ettringite (AFt)[5, 6]; the formed products refine the pore structure[7, 8], and meanwhile accumulate pore pressure high enough to swell the material and deteriorate the mechanical properties[9, 10]. Among the obtained knowledge, the acceleration nature of leaching in ESA damage has been highlighted: Brown[11] found that ESA in neutral aqueous solution (pH=7) has a faster expansion rate and more loss of strength compared to ESA in aqueous solutions without controlling the acidity (alkalinity); Xiong and Jiang[12] reported more severe loss of Vickers hardness for cement pastes under the combined actions of leaching and ESA than those subject to leaching or ESA alone. In fact, the leaching is the most common accompanying process of ESA in aqueous sulfate-containing environments, such as seawater and groundwater, or in laboratory study with frequent replacement of sulfate solution. Thus, it is essential to take into account this factor for service life prediction of concretes exposed to ESA.

On the basis of available knowledge, the role of leaching in ESA damage of concretes can be summarized as follows: the ion species in pore solution, mainly calcium and hydroxide ions (Ca^{2+}, OH^-), transport outwards to external neutral environments through the aqueous phase; this transport process alters the ionic environment in pore solution and breaks the dissolution equilibria of solid phases of cement-based matrix, including both the cement hydrates such as the portlandite (CH) and the calcium silicate hydrates (CSH), and the products of sulfate reactions such as gypsum and ettringite (AFt) [13, 14, 15]; and meanwhile the dissolution of solid phases changes the pore structure, ionic diffusivity and strength of material [16, 17, 18, 19]. On material level, this aspect has been captured by several models considering the combined actions of leaching and ESA: Bary et al.[20, 21] related the loss of mechanical properties to the CSH decalcification and the formation of expansive products to the extent of calcium

*Corresponding author
thumbnails/cas-email.jpeg (K. LI)
ORCID(s): 0000-0003-1635-6362 (K. LI)

leaching; Cefis and Comi[22] decoupled the chemical and mechanical damages caused by leaching and ESA, and revealed qualitatively the existence of mechanical damage depth beneath the chemical one; Qin et al.[23] investigated the impact of ESA and leaching on material expansion through a chemo-transport-damage model and confirmed the mutual acceleration nature between ESA and leaching. These models elaborated most of knowledge available for ESA and leaching and reproduced satisfactorily of relevant material expansion results while a generalized and simplified model for engineering use is still missed. Actually, due to the much larger dimension of concrete surface compared to the ESA/leaching penetrating depth, the damage pattern in real sulfate-containing environments is usually manifested as concrete surface spalling rather than volumetric swelling as usually characterized in laboratory [12, 24, 25, 26]. This damage pattern has been addressed by earlier works from Atkinson and Hearne[27] but no leaching effect was considered.

This paper continues to explore this damage pattern for engineering use and attempts to propose simplified models, in parallel to the sophiscated multi-field modeling, to address the spalling rate of concrete subject to ESA and leaching. The models will incorporate the best knowledge of sulfate reactions and the pore-level consequence, and, if possible, obtain analytical solutions instead of numerical ones. In doing so, some simplifications are inevitable, e.g. the contribution of gypsum to sulfate reactions is neglected. The pore species transport is described by the sulfate and hydroxide ions through a dual moving boundary problem (MBP). The pore stress is estimated through poromechanics for ettringite crystallization in pores. Together with the adopted fracture criterion, the spalling depth is solved. Following this line, this paper is organized as follows: the spalling rate models are presented in Section 2; the model validations are given in Section 3 for spalling depths; the further parametric analysis is provided in Section 4; and the concluding remarks are summarized in Section 5.

2. Spalling rate model

2.1. Statement of problem

The combined action of ESA and leaching is illustrated in Figure 1 as a uni-dimensional problem in semi-infinite domain with given sulfate concentration and neutral pH value on the concrete surface. The concrete is regarded to be totally saturated by aqueous phases. The ionic transport is described by the inward diffusion of sulfate ions (ESA) and outward diffusion of hydroxide ions, cf. Figure 1a,b. The existence and stability of AFt crystals, ettringite, is determined through its supersaturation degree, β_{AFt}, in the aqueous pore solution. The newly formed ettringite after concrete

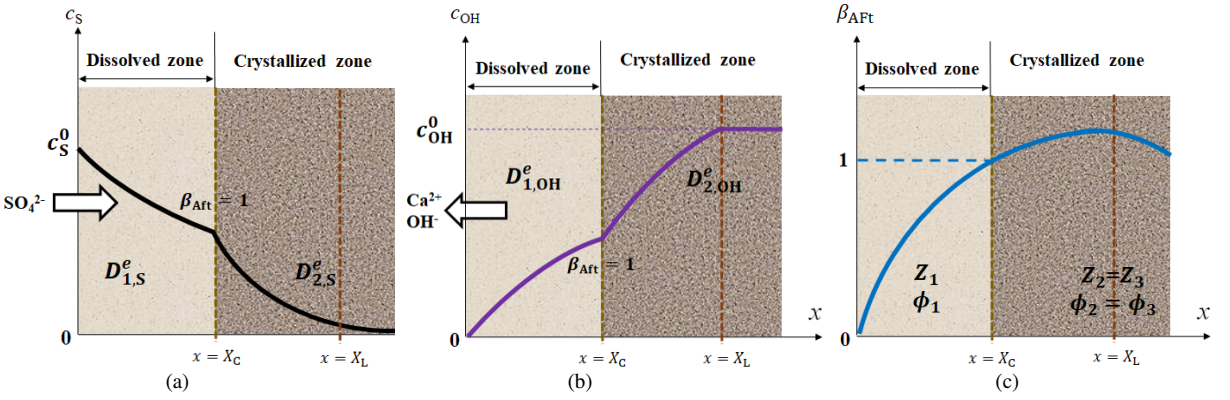

Figure 1: Transport and ionic distribution during ESA and leaching: (a) sulfate ions transport inwards across (AFt-)dissolved zone and (AFt-)crystallized zone; (b) hydroxide ions transport outwards across the crystallized and dissolved zones; (c) supersaturation degree distribution of AFt. The terms $D^e_{1,2;S,OH}$ stand for the effective diffusivities of SO_4^{2-} and OH^- for dissolved and crystallized zones, $\phi_{1,2}$ refer to the porosities of the two zones, $X_{C,L}$ represent the crystallization and leaching fronts, $C^0_{S,OH}$ are boundary SO_4^{2-} concentration and OH^- concentration of intact pore solution respectively. The term β_{AFt} denotes the supersaturation of AFt in aqueous solution.

hardening is assumed to be produced from the chemical reaction between the external sulfates and the hydrogarnets C_3AH_6, the most stable form of aluminum hydrates[28],

$$C_3AH_6 + 3Ca^{2+} + 3SO_4^{2-} + 26H_2O \rightarrow C_3A(\overline{CS})_3H_{32} \tag{1}$$

and the supersaturation degree of AFt writes,

$$\beta_{\mathrm{AFt}} = \frac{a^6_{\mathrm{Ca}^{2+}} a^2_{\mathrm{Al(OH)_4^-}} a^4_{\mathrm{OH}} a^3_{\mathrm{S}}}{K_{\mathrm{AFt}}} \tag{2}$$

with K_{AFt} standing for dissolution constant of AFt and a_i the ionic activity for species i (mol/m^3). The dilute solution is assumed for concrete pore solution, taking the ionic activity a_i numerically equal to the ionic concentration c_i.

Under these circumstances, the concrete can be divided into several zones following the sulfate ingress direction: the dissolved zone (Z_1) where the formed ettringite dissolves due to the outward diffusion of OH^- ions with $\beta_{\mathrm{AFt}} < 1$[29], the crystallized zone (Z_2) where enough sulfate ions exist with $\beta_{\mathrm{AFt}} \geq 1$. In the deeper part of crystallized zone (Z_2), the pore solution is not yet perturbed by the leaching, i.e. the OH^- ions remain at the intact level for pore solution, corresponding to the intact zone with respect to leaching but not necessarily to sulfate ingress. This part is denoted as the intact zone (Z_3). Some lengths are defined accordingly: X_C refers to the crystallization front, delimiting the zones $Z_{1,2}$; X_L refers to the position of leaching front [30, 31], positioning the Z_3 zone. For easier notation, the zone Z_2 refers to only the part between X_C and X_L hereafter. Using the definition of supersaturation β_{AFt} in Eq.(2), one can make the following judgements: it will increase from the concrete surface to deeper part of Z_1 due to the increasing of OH^- concentration with depth, it will decrease after $x > X_L$ due to the decreasing of sulfate concentration and stable concentrations of other ions, and a maximum supersaturation must exist in Z_2 if the crystallization of ettringite has ever occurred, cf. Figure 1c. In other words, these lengths observe

$$\beta_{\mathrm{AFt}} = 1 \ : \ x = X_C \quad \text{and} \quad X_C \leq X_L \tag{3}$$

To build a solvable problem, we make further assumptions for the leaching and related physical properties for these three zones. For leaching, only the dissolution equilibrium of CH is taken into account and the buffering effect of CSH for Ca^{2+} and OH^- ions in pore solution is neglected. The analytical solutions of leaching front X_L are available following such assumptions [30, 31]. For solid phases, Z_1 contains neither AFt nor CH, Z_2 contains AFt but no CH, and Z_3 contains CH and AFt if the supersaturation in Eq.(2) reaches 1. For porosity in different zones, the porosity ϕ_1 in Z_1 corresponds to the concrete totally leached, the porosity ϕ_2 in Z_2 corresponds to leached concrete with pores refilled by ettringite crystals, and the porosity ϕ_3 in Z_3 to the intact concrete with possible AFt formation. Following this argument, the porosity and transport properties are assumed to observe

$$\phi_1 = \mathrm{const}, \phi_2 = \phi_3 = \mathrm{const} \quad \text{and} \quad D^e_{1,2;i} = \mathrm{const}. \tag{4}$$

with $D^e_{1,2;i}$ representing effective diffusivities of i ion in Z_1 and Z_2 respectively.

2.2. Diffusion of sulfate and hydroxide ions

The mass conservation of sulfate ions writes,

$$\frac{\partial C_S}{\partial t} = D^e_S \frac{\partial^2 c_S}{\partial x^2} \quad \text{with} \quad C_S = \phi c_S + n_S \tag{5}$$

where C_S and n_S represent the total sulfates in concrete (mol/m^{3}concrete) and the bound sulfates in AFt (mol/m^{3}concrete), D^e_S denotes the effective sulfate diffusivity (m^2/s), and ϕ the concrete porosity. Using the second part of equation, the mass conservation can be rewritten using aqueous sulfate concentration c_S as basic variable,

$$\frac{\partial c_S}{\partial t} = D_S \frac{\partial^2 c_s}{\partial x^2} \quad \text{with} \quad D_S = \frac{D^e_S}{\phi + n'_S} \tag{6}$$

Here n'_S denotes the derivative of n_S with respect to c_S, and D_S stands for the apparent sulfate diffusivity, combining the pore diffusion and the chemical AFt formation. Retaining Eq.(6) as basic expression, the sulfate transport in $Z_{1,2}$ zones write,

$$\begin{cases} \dfrac{\partial c_S}{\partial t} = D_{1,S}\dfrac{\partial^2 c_S}{\partial x^2}, \quad x < X_C \quad \text{with} \quad D_{1,S} = \dfrac{D^e_{1,S}}{\phi_1 + n'_S},\ n'_S = 0 \\ \dfrac{\partial c_S}{\partial t} = D_{2,S}\dfrac{\partial^2 c_S}{\partial x^2}, \quad x \geq X_C \quad \text{with} \quad D_{2,S} = \dfrac{D^e_{2,S}}{\phi_2 + n'_S} \end{cases} \tag{7}$$

with $D_{1,2;S}$ denoting the apparent sulfate diffusivities in dissolved and crystallized zones respectively. Further, a linear relation is assumed between the bound sulfates n_S and aqueous sulfate concentration c_S, leading to constant apparent sulfate diffusivity in Z_2, i.e.

$$n_S = \phi_2 r_S c_S n_{C_3AH_6} : \quad D_{2;S} = \text{const} \tag{8}$$

where $n_{C_3AH_6}$ is the available content of aluminum hydrates (mol/m^3 concrete), and r_S a chemical factor related to AFt formation. The initial and boundary conditions write,

$$\begin{cases} c_S(x > 0, t = 0) = 0,\ c_S(x = 0, t > 0) = c^0_S \\ c_S|_{x=X^-_C} = c_S|_{x=X^+_C},\ D_{1,S}\dfrac{\partial c_S}{\partial x}\Big|_{x=X^-_C} = D_{2,S}\dfrac{\partial c_S}{\partial x}\Big|_{x=X^+_C} \end{cases} \tag{9}$$

with c^0_S representing boundary sulfate concentration in external environment. The second expression depicts the concentration continuity and mass conservation of aqueous sulfates across the crystallization front X_C.

Also derived from the mass conservation, the hydroxide diffusion in the dissolved, crystallized and intact zones writes,

$$\begin{cases} \dfrac{\partial c_{OH}}{\partial t} = D_{1,OH}\dfrac{\partial^2 c_{OH}}{\partial x^2}, & x < X_C \\ \dfrac{\partial c_{OH}}{\partial t} = D_{2,OH}\dfrac{\partial^2 c_{OH}}{\partial x^2}, & X_C \leq x < X_L \\ \dfrac{\partial c_{OH}}{\partial t} = 0, & x \geq X_L \end{cases} \tag{10}$$

with $D_{1,2;OH}$ representing the apparent hydroxide diffusivities in $Z_{1,2}$ respectively. The initial and boundary conditions write,

$$\begin{cases} c_{OH}(x = 0, t > 0) = 0, \quad c_{OH}(x \geq X_L) = c^0_{OH} \\ c_{OH}|_{x=X^-_C} = c_{OH}|_{x=X^+_C}, \quad D_{1,OH}\dfrac{\partial c_{OH}}{\partial x}\Big|_{x=X^-_C} = D_{2,OH}\dfrac{\partial c_{OH}}{\partial x}\Big|_{x=X^+_C} \\ n_{CH}\dfrac{dX_L}{dt} = -\phi_2 D_{2,OH}\dfrac{\partial c_{OH}}{\partial x}\Big|_{x=X_L} \end{cases} \tag{11}$$

with c^0_{OH} standing for OH^- concentration in intact pore solution, n_{CH} denoting CH content (mol/m^{3}concrete). The second expression describes the concentration continuity and mass conservation of aqueous hydroxide ions across X_C, and the third expression depicts the mass conservation of hydroxide ions across the leaching front X_L.

2.3. Solution of crystallization front through dual moving boundary problem

The Eqs.(7)-(11) constitute a dual moving boundary problem (MBP) for combined ESA and leaching. In 1D semi-infinite domain, a single MBP, with fixed concentration at external boundary and mass continuity across the moving boundary, provides the moving rate of boundary proportional to square root of time [32, 33]. On this basis, we express

the crystallization front X_{C} and leaching front X_{L} in terms of square root of time with their respective rate coefficients,

$$X_{\mathrm{C}} = k\sqrt{t}, \quad X_{\mathrm{L}} = \kappa\sqrt{t} \quad \text{with} \quad k \le \kappa \tag{12}$$

with k and κ denoting the moving rates for the crystallization and leaching fronts (m/s$^{0.5}$). As long as the two rate coefficients can be determined uniquely using the conditions in this dual MBP, the above expression can be proved to be the correct solution for $X_{\mathrm{C,L}}$, which will be demonstrated later in this section. On the basis of above linear relations, the general solution takes the following form with the mathematical details given in Appendix A,

$$\begin{cases} \dfrac{c_{\mathrm{S}}}{c_{\mathrm{S}}^0} = A_1 \mathrm{erfc}\left(\dfrac{x}{2\sqrt{D_{1,\mathrm{S}}t}}\right) + A_2, & \dfrac{c_{\mathrm{OH}}}{c_{\mathrm{OH}}^0} = a_1 \mathrm{erf}\left(\dfrac{x}{2\sqrt{D_{1,\mathrm{OH}}t}}\right), & x < k\sqrt{t} \\ \dfrac{c_{\mathrm{S}}}{c_{\mathrm{S}}^0} = A_3 \mathrm{erfc}\left(\dfrac{x}{2\sqrt{D_{2,\mathrm{S}}t}}\right), & \dfrac{c_{\mathrm{OH}}}{c_{\mathrm{OH}}^0} = a_2 \mathrm{erf}\left(\dfrac{x}{2\sqrt{D_{2,\mathrm{OH}}t}}\right) + a_3, & k\sqrt{t} \le x < \kappa\sqrt{t} \\ \dfrac{c_{\mathrm{S}}}{c_{\mathrm{S}}^0} = A_3 \mathrm{erfc}\left(\dfrac{x}{2\sqrt{D_{2,\mathrm{S}}t}}\right), & \dfrac{c_{\mathrm{OH}}}{c_{\mathrm{OH}}^0} = 1, & x \ge \kappa\sqrt{t} \end{cases} \tag{13}$$

with the constants dependent on materials parameters,

$$A_{1,2,3} = A_{1,2,3}(k, D_{1,\mathrm{S}}, D_{2,\mathrm{S}}), \quad \text{and} \quad a_{1,2,3} = a_{1,2,3}(k, \kappa, D_{1,\mathrm{OH}}, D_{2,\mathrm{OH}}) \tag{14}$$

Now we turn to determine the two moving rates using the mass conservation of CH across the leaching front in Eq.(11)$_3$ and the dissolution equilibrium of AFt in Eqs.(2),(3)$_1$. Putting the leaching front in Eq.(12) and the profile of OH^- in Eq.(13) into Eq.(11)$_3$, the mass conservation of CH across the leaching front is expressed in terms of the two rate coefficients k and κ,

$$\kappa \exp\left(\frac{\kappa^2}{4D_{2,\mathrm{OH}}}\right) = \frac{2}{\sqrt{\pi}} \frac{\phi_2 c_{\mathrm{OH}}^0 \sqrt{D_{2,\mathrm{OH}}}}{n_{\mathrm{CH}}} a_2(k, \kappa) \tag{15}$$

The calculation of supersaturation degree of AFt needs to specify the ionic concentrations not explicitly included in Eq.(13), such as $c_{\mathrm{Ca}^{2+}}$ and $c_{\mathrm{Al(OH)}_4^-}$. Actually the two concentrations should satisfy all the dissolution equilibria in multi-species ionic aqueous environment of pore solution[34]. Here for simplification, CH is regarded as the only dissolution source for Ca^{2+} and the two ions, Ca^{2+} and OH^-, transport strictly together. These assumptions lead to,

$$\frac{c_{\mathrm{Ca}^{2+}}}{c_{\mathrm{OH}}} = \frac{c_{\mathrm{Ca}^{2+}}^0}{c_{\mathrm{OH}}^0} = \frac{K_{\mathrm{CH}}}{\left(c_{\mathrm{OH}}^0\right)^3} \tag{16}$$

with $c_{\mathrm{Ca}^{2+}}^0$ and $c_{\mathrm{OH}^-}^0$ as the initial calcium and hydroxide ions concentrations in Z_3. Due to its very small value, the aluminate concentration is considered as a constant by neglecting its pore transport and by assuming $\mathrm{C_3AH_6}$ always available in solid phases. These assumption lead to the aluminate concentration equal to its initial value in Z_3. Together with the only Ca^{2+} source from CH, the aluminate concentration can be expressed as,

$$c_{\mathrm{Al(OH)}_4^-} = c_{\mathrm{Al(OH)}_4^-}^0 = \sqrt{\frac{K_{\mathrm{C_3AH_6}}}{K_{\mathrm{CH}}^3}\left(c_{\mathrm{OH}}^0\right)^5} \tag{17}$$

with $c_{\mathrm{Al(OH)}_4^-}^0$ as the initial concentration in Z_3. Putting Eqs.(16),(17) into Eq.(2) gives the AFt supersaturation,

$$\beta_{\mathrm{AFt}} = K' c_{\mathrm{OH}}^{10} c_{\mathrm{S}}^3 \quad \text{with} \quad K' = \frac{K_{\mathrm{C_3AH_6}} K_{\mathrm{CH}}^3}{K_{\mathrm{AFt}}} \frac{1}{\left(c_{\mathrm{OH}}^0\right)^{13}} \tag{18}$$

Then, substituting the profiles in Eq.(13) into Eq.(18) gives the second relation for the two moving rate coefficients k and κ,

$$\left[a_1(k,\lambda)\mathrm{erf}\left(\frac{k}{2\sqrt{D_{1,\mathrm{OH}}}}\right)\right]^{10}\left[A_3(k)\mathrm{erf}\left(\frac{k}{2\sqrt{D_{2,\mathrm{S}}}}\right)\right]^{3}=\frac{1}{K'} \tag{19}$$

So far, the two moving rate coefficients can be solved through the CH mass conservation and the AFt dissolution equilibrium expressed respectively in Eq.(15) and Eq.(19), which are mathematically solvable. This observation also confirms the correctness of the proportionality between $X_{\mathrm{C,L}}$ and $\sqrt{t}$, taken in Eq.(12). With solved moving rate coefficients, we can determine the profiles in Eq.(13), the parameters in Eq.(14) and the AFt supersaturation profile through Eq.(18), which lays ground for the pore pressure analysis. More generally, any law, which defines the relation between c_{S} and c_{OH} at X_{C}, can serve as the second constraint, in the place of Eq.(19), to solve the two rate coefficients.

2.4. Spalling depth

In this model, we assume that the pore pressure arises from the crystallization of ettringite and constitutes the physical source for concrete expansion and damage. The crystallization pressure, P_{C}, is related to AFt supersaturation through the Correns' equation[35],

$$P_{\mathrm{C}}-P_{\mathrm{L}}=\frac{RT}{V_{\mathrm{C}}}\ln(\beta_{\mathrm{AFt}}) \tag{20}$$

where P_{L} represents liquid pressure (Pa), R stands for the ideal gas constant (J/(mol·K)), T denotes the absolute temperature (K), and V_{C} the molar volume of ettringite crystal (m^3/mol). The poromechanics expresses the effective stress on solid matrix, σ', as[36],

$$\sigma'=\sigma+b(S_{\mathrm{C}}P_{\mathrm{C}}+S_{\mathrm{L}}P_{\mathrm{L}})\quad\text{and}\quad S_{\mathrm{C}}+S_{\mathrm{L}}=1 \tag{21}$$

where σ is the material total (external) stress (Pa), b is the Biot's coefficient, $S_{\mathrm{C,L}}$ are the volume fractions of pore space occupied by the crystals and the liquid respectively. Due to the dissolution of AFt and CH in Z_1, it is assumed that there is no pressure building-up for liquid phase and the liquid pressure is equal to atmosphere pressure. The crystal saturation S_{C} can be evaluated from the bound sulfates content n_{S},

$$S_{\mathrm{C}}=\frac{n_{\mathrm{S}}V_{\mathrm{C}}}{\phi_1}=r_{\mathrm{S}}n_{\mathrm{C_3AH_6}}V_{\mathrm{C}}\frac{\phi_2}{\phi_1}c_{\mathrm{S}} \tag{22}$$

Under a stress-free condition without external loading, the effective stress writes,

$$\sigma=0:\sigma'=\gamma c_{\mathrm{S}}\ln(\beta_{\mathrm{AFt}})\quad\text{with}\quad\gamma=r_{\mathrm{S}}n_{\mathrm{C_3AH_6}}\frac{\phi_2}{\phi_1}bRT \tag{23}$$

2.4.1. Spalling rate without cracking effect on diffusivity

Consider first a uniaxial strain problem. The lateral strains are fixed to zero, $\epsilon_{yy,zz}=0$, and the stress is free in x axis, $\sigma_{xx}=0$, leaving ϵ_{xx} as the only possible strain. Under these conditions, the effective stress in solid matrix along x axis writes,

$$\sigma_{xx}=0:\sigma'_{xx}=\gamma c_{\mathrm{S}}\ln(\beta_{\mathrm{AFt}}) \tag{24}$$

In this case, the tensile stress σ'_{xx} induced by pore crystallization is the only cause of fracture of solid matrix and the cracks induced by the pore crystallization are assumed to be arranged perpendicular to x axis, corresponding to the layered spalling damage pattern. This pattern most probably occurs for elements such as walls with very large (infinite) surface, perpendicular to x axis, of which the in-place strains $\epsilon_{yy,zz}$ can be assumed to be cancelled out. Under this cracking pattern, the ionic diffusivity remains unaffected in the sulfate penetration direction. Holding this assumption and using the expression in Eq.(24), we can express the effective stress σ'_{xx} through the Boltzmann variable η in Eq.(A.1),

$$\sigma'_{xx}=\begin{cases}0, & 0\le\eta<k\\ \gamma c_{\mathrm{S}}^{0}A_3\mathrm{erfc}\left(\dfrac{\eta}{2\sqrt{D_{2,\mathrm{S}}}}\right)\ln\left\{K'\left[a_2\mathrm{erf}\left(\dfrac{\eta}{2\sqrt{D_{1,\mathrm{OH}}}}\right)+a_3\right]^{10}\left[A_3\mathrm{erfc}\left(\dfrac{\eta}{2\sqrt{D_{2,\mathrm{S}}}}\right)\right]^{3}\right\}, & k\le\eta<\kappa\\ \gamma c_{\mathrm{S}}^{0}A_3\mathrm{erfc}\left(\dfrac{\eta}{2\sqrt{D_{2,\mathrm{S}}}}\right)\ln\left\{K'\left[A_3\mathrm{erfc}\left(\dfrac{\eta}{2\sqrt{D_{2,\mathrm{S}}}}\right)\right]^{3}\right\}, & \eta\ge\kappa\end{cases}\tag{25}$$

The fracture criterion is simply taken as the effective stress σ'_{xx} attaining the tensile strength of concrete σ_{ft}. Considering Eq.(25), the spalling rate coefficient η' can be solved,

$$\sigma'_{xx}(\eta=\eta')=\sigma_{\mathrm{ft}}:\quad \eta'=\frac{X_{\mathrm{spalling}}}{\sqrt{t}}\tag{26}$$

where X_{spalling} stands for the spalling depth by ESA and leaching action. This solution reveals that, like crystallization front and leaching front, the spalling depth is also proportional to the square root of time.

2.4.2. Spalling rate with cracking effect on diffusivity

Here we release the conditions of zero lateral strains in the precedent uniaxial strain problem and replace by free stress conditions $\sigma_{yy,zz}=0$, making $\epsilon_{yy,zz}$ as possible strains. Under these conditions, the effective stress in lateral directions writes,

$$\sigma_{yy,zz}=0:\sigma'_{yy,zz}=\gamma c_{\mathrm{S}}\ln(\beta_{\mathrm{AFt}})\tag{27}$$

In this case, the tensile stress $\sigma'_{yy,zz}$ induced by the pore crystallization can cause the fracture of solid matrix when reaching σ_{ft}. This fracture process will generate cracking parallel to the x axis, possibly together with the spalling pattern of cracking. This pattern may occur for elements such as beams and columns with finite size of surface, perpendicular to the x axis, and bearing the free lateral surface, where the lateral stress $\sigma_{yy,zz}$ can be assumed to be zero.

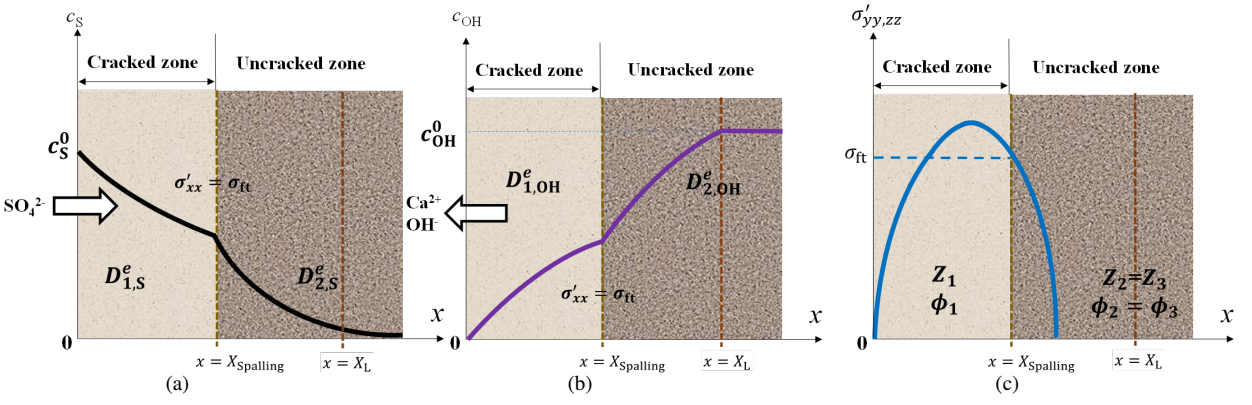

Figure 2: Transport and ionic distribution during ESA and leaching considering cracks: (a) sulfate ions transport inwards across spalling-cracking zone and uncracked zone; (b) hydroxide ions transport outwards across the uncracked zone and spalling-cracking zone; (c) effective stress distribution. The terms $D^{e}_{1,2;\mathrm{S,OH}}$ stand for the effective diffusivities of SO_4^{2-} and OH^- for spalling-cracking zone and uncracked zone, $\phi_{1,2}$ refer to the porosities of the two zones, $X_{\mathrm{spalling,L}}$ represent the spalling and leaching fronts, $C^{0}_{\mathrm{S,OH}}$ are boundary SO_4^{2-} concentration and OH^- concentration of intact pore solution, and σ'_{xx} and σ_{ft} denote effective stress and tensile strength of concrete respectively.

Another particular case for this pattern refers to the 1D diffusion-crystallization process in axisymmetric coordinates where the hooping (circumferential) tensile stress in solid matrix dominates over other stress components and induces cracking parallel to the radical axis.

Since the presence of parallel cracks affect substantially the ionic diffusivity in the x axis direction, we need to adapt the dual MBP illustrated in Figure 1 to spalling-cracking case illustrated in Figure 2 to evaluate the spalling depth and rate: the zones $Z_{1,2,3}$ represent now the spalling-cracking zone, the un-cracked zone and the intact zone by leaching. The delimiting lengths are spalling depth X_{spalling} and leaching depth X_{L}. Like the solution to the original dual MBP, we assume,

$$X_{\text{Spalling}} = \eta'\sqrt{t}, \quad X_{\text{L}} = \kappa\sqrt{t} \tag{28}$$

We can substitute η' for k in the original MBP and solve the new problem following the same procedure as Section 2.3 and the sulfate and hydroxide profiles take the same form as in Eq.(13). The only difference is the determination of the two new moving rate coefficients η' and κ. Instead of using the CH mass conservation and AFt dissolution equilibrium, the CH mass conservation and fracture criterion are used for their determination. And in this case, unlike in Eq.(12), the spalling-cracking front X_{spalling} can surpass the leaching front X_{L}, cancelling out the zone Z_2.

As $X_{\text{spalling}} < X_{\text{L}}$, the relations for solving the two moving rate coefficients are constituted by Eq.(15) and Eq.(27) using the fracture criterion $\sigma'_{yy,zz} = \sigma_{\text{ft}}$,

$$\begin{cases} \kappa\exp\left(\dfrac{\kappa^2}{4D_{2,\text{OH}}}\right) = \dfrac{2}{\sqrt{\pi}}\dfrac{\phi_2 c^0_{\text{OH}}\sqrt{D_{2,\text{OH}}}}{n_{\text{CH}}}a_2(\eta',\kappa) \\ \sigma_{\text{ft}} = \gamma c^0_{\text{S}} A_3(\eta')\text{erfc}\left(\dfrac{\eta'}{2\sqrt{D_{2,\text{S}}}}\right)\ln\left\{K'\left[a_1(\eta',\kappa)\text{erf}\left(\dfrac{\eta'}{2\sqrt{D_{1,\text{OH}}}}\right)\right]^{10}\left[A_3(\eta')\text{erfc}\left(\dfrac{\eta'}{2\sqrt{D_{2,\text{S}}}}\right)\right]^{3}\right\} \end{cases} \tag{29}$$

As $X_{\text{spalling}} \geq X_{\text{L}}$, the two relations still come from the same expressions but totally decoupled,

$$\begin{cases} \kappa\exp\left(\dfrac{\kappa^2}{4D_{1,\text{OH}}}\right) = \dfrac{2}{\sqrt{\pi}}\dfrac{\phi_2 c^0_{\text{OH}}\sqrt{D_{1,\text{OH}}}}{n_{\text{CH}}}a_2(\kappa) \\ \sigma_{\text{ft}} = \gamma c^0_{\text{S}} A_3(\eta')\text{erfc}\left(\dfrac{\eta'}{2\sqrt{D_{2,\text{S}}}}\right)\ln\left\{K'\left[A_3(\eta')\text{erfc}\left(\dfrac{\eta'}{2\sqrt{D_{2,\text{S}}}}\right)\right]^{3}\right\} \end{cases} \tag{30}$$

Again, the unique determination of the two moving rate coefficients confirms the correctness of the relations taken in Eq.(28) for the new dual MBP problem. The spalling depth is also proportional to the square root of time.

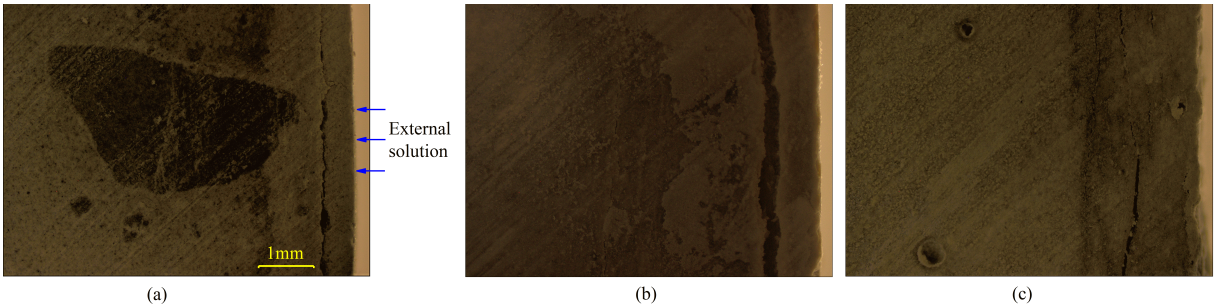

Figure 3: Cracking observation on cross sections of cement paste disks (w/c=0.55) by optical microscope for (a) 8-week, (b)16-week and (c) 32-week immersion in sodium sulfate solution of 10g/L SO_4^{2-} with pH value controlled to 7.0±0.1. Right edge of each image is the exposure surface.

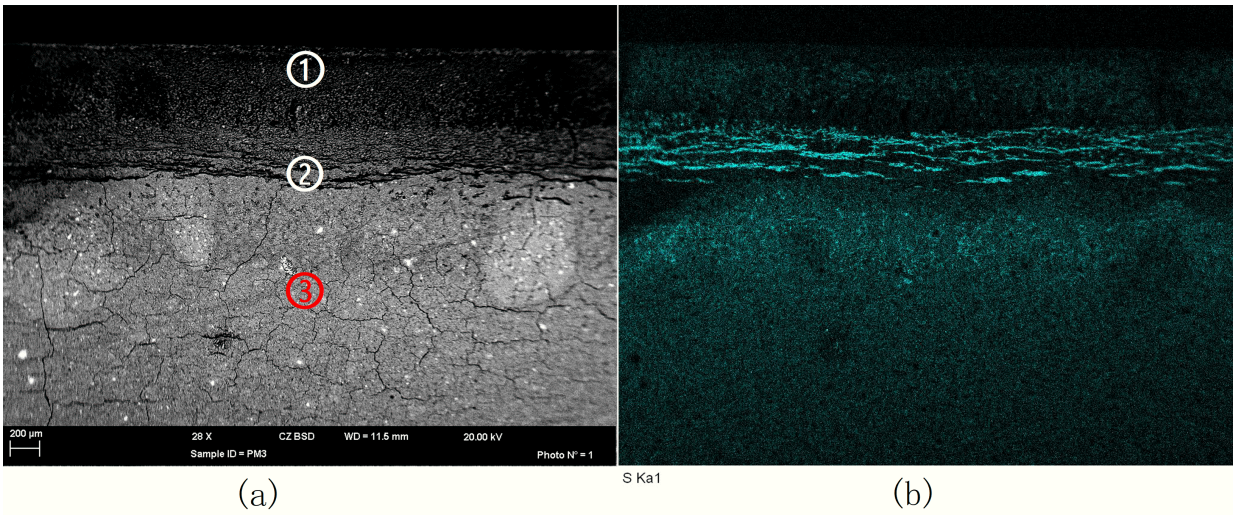

Figure 4: BSE (a) and sulfur element mapping (b) images on cross sections of cement paste disks (w/c=0.55) immersed in sodium sulfate solution of 10g/L SO_4^{2-} for 8 weeks. Top edge of each image is the exposure surface.

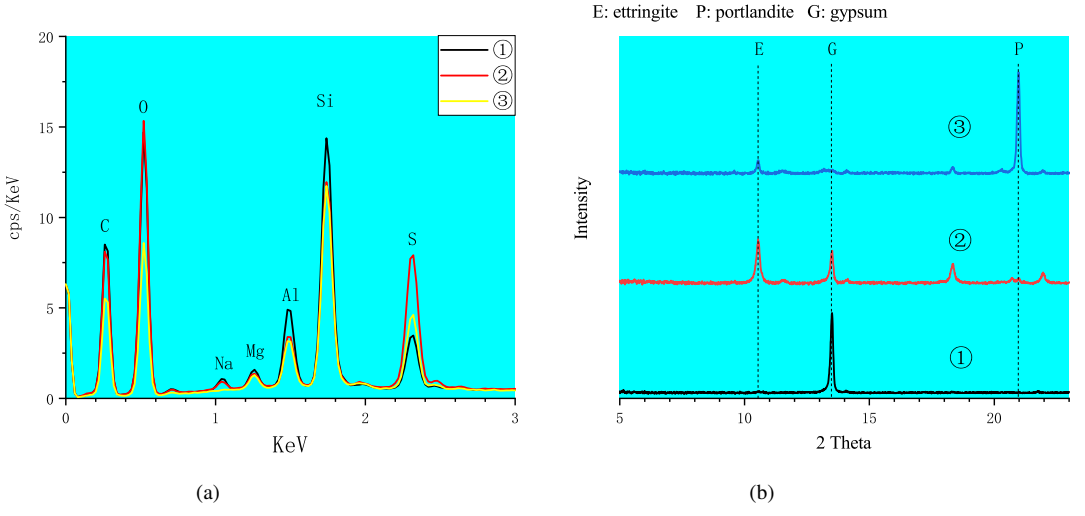

Figure 5: EDS (a) and XRD (b) results of cement paste disks (w/c=0.55) immersed in sodium sulfate solution of 10g/L SO_4^{2-} for 8 weeks using the samples from the three marked positions in Figure 4a.

3. Validation

3.1. Disk specimens

Cylinders of 11cm diameter and 22cm height were made from cement paste with a water to cement ratio (w/c) of 0.55. The cement used is CEM I Type (CEMI 52.5 N CE CP2). After 60d curing in saturated CH solution, disk specimens of 5cm height were sawed out from cylinders, and epoxy resin was applied on the lateral and bottom surfaces of disk specimens to leave the top surface exposed to external sulfate penetration. The disks were then immersed into a Na_2SO_4 solution of 10g/L sulfate, and a pH regulator was adopted to maintain pH=7.0 $\pm$ 0.1 for the test solution, which was replaced every two weeks to ensure a consistent sulfate concentration [5].

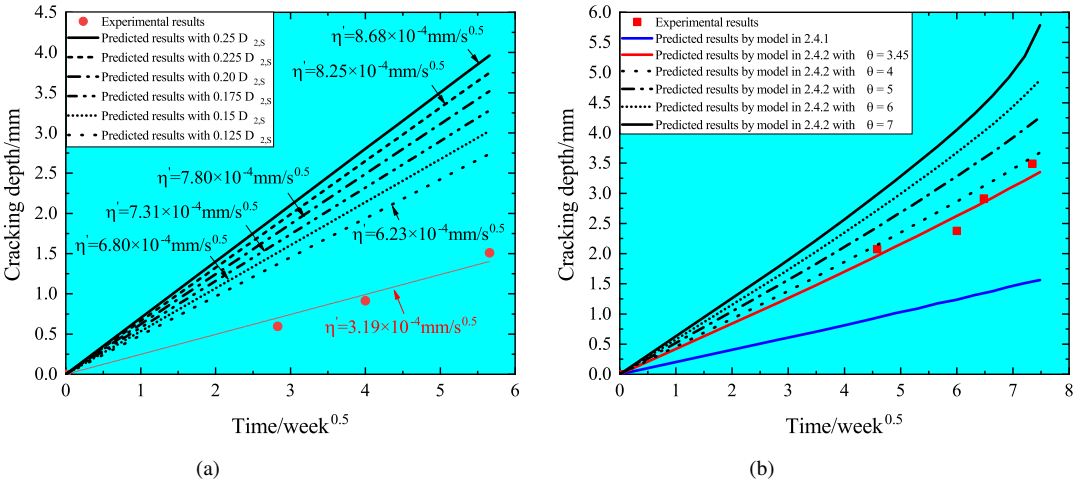

Figure 6: Cracking depth measured in experiments and spalling rate predicted by models for (a) disk cement paste specimens (w/c=0.55)immersed in sodium sulfate solution of 10g/L SO_4^{2-}, and (b) small cylinder cement paste specimens (w/c=0.485) exposed to 10g/L SO_4^{2-} in sodium sulfate solution[15]. θ is the magnification coefficient of apparent diffusivities in the cracked zone in Figure 2.

After being exposed to sulfate solution for 8, 16, and 32 weeks, the disk specimens were cut diametrically to obtain the diffusion direction cross-section. These cross-sections were observed by optical microscope, as shown in Figure 3. The cracks are almost parallel to exposure surface, and the measured cracking depths are given in Figure 6a in terms of the exposure time. The 8-week specimen was polished to conduct the back-scattered electron (BSE) image and the energy dispersive spectroscopy (EDS) mapping tests, and the results are provided in Figure 4. Figure 4a reveals that the single large crack in Figure 3a is actually composed of multiple tiny cracks, and Figure 4b shows how the sulfur element (S) is distributed in three zones: the surface zone with low sulfur content, the cracking zone rich in sulfur element, and the inner zone with a sulfur amount decreasing with depth. The very low content of sulfur element in surface zone supports the assumption that the bound sulfates in solid phases, in AFt, are dissolved by lower pH value, cf. Figure 1c. Further, powder samples were taken from the three zones, with their positions marked in Figure 4a, and subject to analysis of EDS and X-ray diffraction (XRD). The analysis results are given in Figure 5, and the EDS results in Figure 5a confirm the change of sulfur element in the three zones in Figure 4b. From the XRD results in Figure 5b, the surface zone contains only gypsum, the cracking zone beneath contains small amount of portlandite and gypsum but an important quantity of ettringite, and the deeper zone contains small amount of ettringite but large amount of portlandite. Actually these three zones correspond to the zones $Z_{1,2,3}$ in Figure 1. The clear reduction of portlandite peaks from the inner zone to the surface zone confirms the effect of leaching with depth. Comparing the ettringite and gypsum peaks in surface zone and cracking zone indicates that the ettringite is transformed into gypsum in the surface zone.

Due to the damage pattern of layered spalling in Figure 3a-c, we adopt the spalling rate model without cracking effect on diffusivity in Section 2.4.1 for model validation, with the material parameters provided in Table 1. The chemical reaction coefficient r_S is calibrated from the works in [5], where the AFt amount was quantified through ^{27}Al Nuclear Magnetic Resonance (NMR). The contents of cement hydrate phases, n_{CH} and $n_{C_3AH_6}$, were determined from the mineral composition of cement and w/c ratio, following the method in [37]. The initial porosity ϕ_0 was measured by the mercury intrusion porosimetry (MIP), and porosity values in dissolved zone ϕ_1 and crystallized zone ϕ_2 were calculated from the pore release volume by CH dissolution and pore-filling volume by AFt formation. Using these values of porosity, the apparent diffusivities for sulfate and hydroxide ions in the two zones were evaluated through porosity-based models in Appendix B [38]. Literature has reported the rapid reduction of diffusivity, i.e. ageing effect

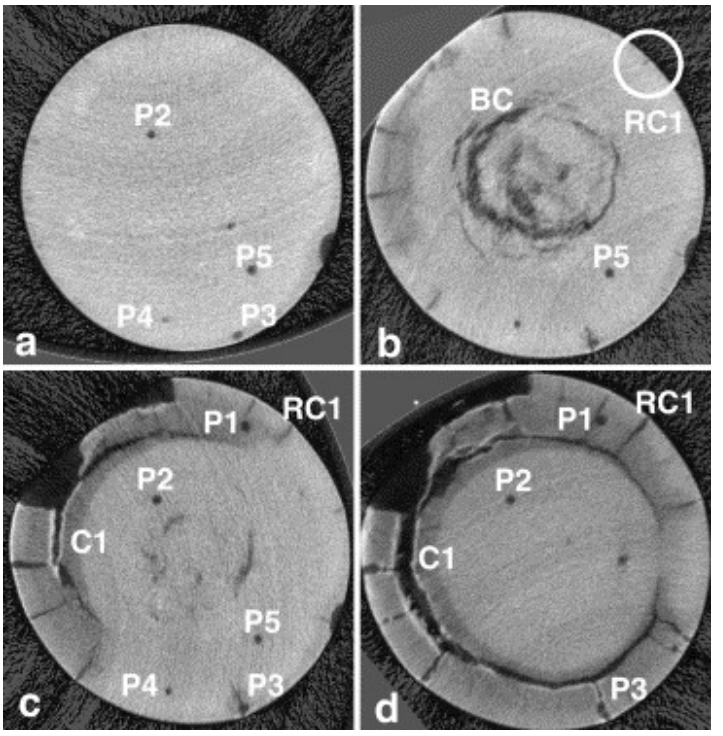

Figure 7: Cracking observation by microCT for Type I cement paste specimens (w/c=0.485) exposed to sodium sulfate solution of 10g/L SO_4^{2-} for (a) 21 weeks, (b) 36 weeks, (c) 42 weeks and (d) 52 weeks. The symbol C1 and RC1 stand for ring crack and radical crack, P1-P5 represent voids, and the field of view is 15.3mm(a), 15.1mm(b), 16.1mm(c) and 15.2mm(d). Source: images adapted from [29], Fig. 12. Reproduced with permission of Elsevier.

of diffusivity, in the early phase of ESA [5]. To account for this important change, a discount ratio of 1/8-1/4 is applied to the computed apparent diffusivities in the crystallized zone on the basis of experimental observations in [15, 39].

The model prediction and the measured spalling (cracking) depths are given in Figure 6a. From the experimental results, a linear relation does exist between the spalling (cracking) depth and the square root of exposure time. Accordingly, the proportionality between X_C and $\sqrt{t}$ is validated, confirming that the spalling damage is dominated by diffusion process. For the predicted and measured values of spalling depth, the two groups of values are at the same order of magnitude, and the predicted values are systematic larger than the measured values. Apart from the various sub-models borrowed from literature, the main reason behind is the neglected buffering effect of CSH on leaching. Actually the CSH can provide both Ca^{2+} and OH^- ions into pore solution as CH is consumed out, and this effect can notably slow down the leaching front[31]. Nevertheless, this overestimation can be acceptable for engineering use which prefers conservative results.

3.2. Small cylinder specimens

Naik et al.[15] prepared cylinder cement paste specimens with diameter of 12.5mm and length of 45mm. The specimens were cast in ASTM type I Portland cement with a w/c ratio of 0.485. The small cylinders were sealed with parafilm and cured in a saturated lime bath for 1d, then demoulded and cured in a saturated lime bath for 2d. The cured samples were then immersed into sodium sulfate solution containing 10g/L sulfate, and the test solution was replaced on a weekly basis. After being exposed to sulfate solution for 21, 36, 42 and 52 weeks, the cylinder specimens were taken out for crack observation through X-ray microtomography (microCT) method, as shown in Figure 7. The measured values for cracking (spalling) depth are given in Figure 6b.

From the microCT images in Figure 7, the damage pattern includes obvious radical cracks. These cracks will provide more direct transport channel for external ions than the capillary pores, and this cracking impact should be considered in model validation. To this aim, the spalling rate model with cracking effect on diffusivities, in Section 2.4.2, is adopted to simulate the damage behaviors of the small cylinder specimens. Another issue to perform the

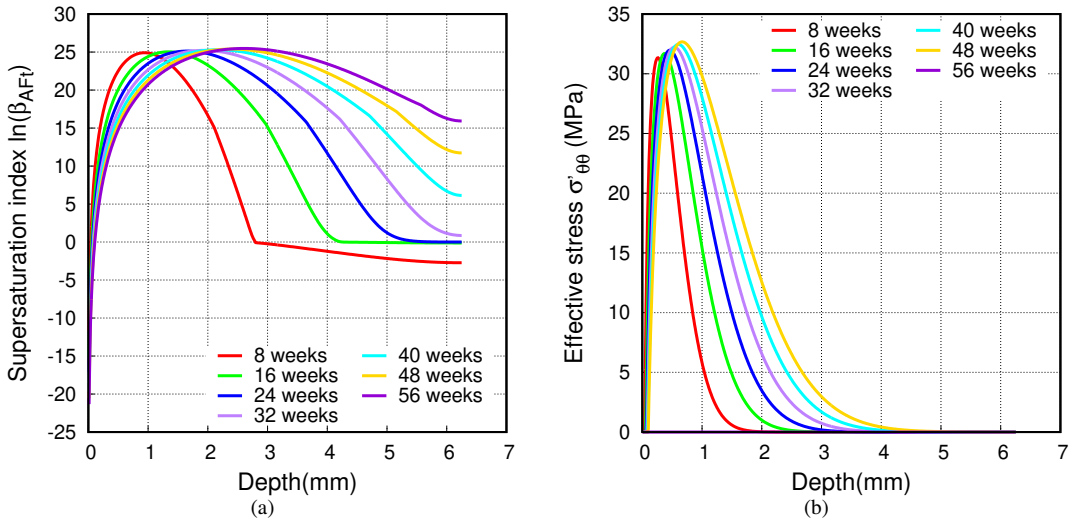

Figure 8: Profiles of AFt supersaturation (a) and effective stress in tension (b) predicted by spalling rate model for small cylinder specimens (w/c=0.485) exposed to sodium sulfate solution containing 10g/L SO_4^{2-}.

analysis involves the coordinate system: the spalling rate model expressed in 1D semi-infinite domain should be converted to 1D axis-symmetric coordinate. The mathematical expression is given in Appendix C. Since there is no explicit analytical solution for the spalling depth X_C in 1D axis-symmetric coordinate, the spalling rate model is solved numerically through the platform Bil[40]. Table 1 lists all the parameters needed in the spalling rate model except the impact of cracking on the diffusivity value in Z_1 zone. A magnification factor, θ, is adopted here to quantify the cracking effect on diffusivity in Z_1,

$$\theta = \frac{D_{1,S}}{D_{2,S}} = \frac{D_{1,OH}}{D_{2,OH}} > 1 \tag{31}$$

Gérard and Marchand[41] measured the parameter θ in the range of 4-7 on cracked disk specimens, and this value range is adopted to simulate the spalling depths. The results are given in Figure 6b and this figure also includes the simulation results from the spalling rate model without cracking effect on diffusivity in Section 2.4.1. From these results, some observations can be made: first, the cracking effect should be taken into account otherwise the spalling depth will be largely underestimated; second, the spalling rate model considering the cracking effect, with reasonable values for the magnification factor, successfully reproduces the spalling depths. Again, the conservative results with correct magnitude order are obtained from the model predictions. The supersaturation degree β_{AFt} and the effective stress σ'_{xx} are calculated and shown in Figure 8 for θ=4. The results show that both the supersaturation and the effective stress have an extremum (local maximum), and within 8-week immersion the supersaturation and effective stress accumulate to high values within 1-2mm from the surface. Note that the large values in Figure 8(b) do not refer to the actual levels of tensile stress in the solid matrix which will be released by fracture. With 1D axis-symmetry transformation and reasonable assumption for cracking impact on diffusivities, the results in Figure 6b confirm the concept of spalling depth and validate the related modeling.

4. Further discussion

4.1. Parameter analysis

Multiple parameters intervene in the spalling rate models in Eq.(26) and Eq.(29). This section is dedicated to the analysis of key parameters to obtain some generalized observations using these models. Conceptually, the spalling rate scales to four groups of parameters: the ionic diffusivity in different zones, the surface boundary ionic concentrations, the chemical contents in concrete, and the mechanical properties related to crystallization and fracture, i.e.

$$\eta' = f\left(D_{1,S}, D_{2,S}; D_{1,OH}, D_{2,OH}; c_S^0, c_{OH}^0; n_{CH}, n_{C_3AH_6}; \sigma_{ft}, \frac{RT}{V_C}\right) \tag{32}$$

The number of basic dimensions is three: length(L), mass(M) and time (T). Note that the absolute temperature T is combined into the variable group RT/V_C and the dimension is cancelled out. According to the Buckingham theorem[42], eight independent dimensionless quantities exist and Eq.(32) can be converted into a function of these eight dimensionless quantities. We retain the hydroxide diffusivity in dissolved zone $D_{1,OH}$, boundary hydroxide concentration c_{OH}^0 and tensile strength σ_{ft} as basic variables, and express Eq.(32) through the following dimensionless quantities,

$$\begin{aligned} &\eta^- = f'\left(D_S^-, k_1, \frac{D_S^-}{K_1}; c_S^-, \frac{n_{CH}}{c_{OH}^0}, \frac{n_{C_3AH_6}}{c_{OH}^0}; \frac{\sigma_{ft}V_C}{RT}\right) \\ &\text{with} \quad \eta^- = \frac{\eta'}{2\sqrt{D_{1,OH}}}, D_S^- = \sqrt{\frac{D_{2,S}}{D_{1,OH}}}, k_1 = \sqrt{\frac{D_{2,OH}}{D_{1,OH}}}, K_1 = \sqrt{\frac{D_{1,S}}{D_{2,S}}}, c_S^- = \frac{c_S^0}{c_{OH}^0}, \end{aligned} \tag{33}$$

Table 1
Parameters adopted in the spalling rate models

Parameter(unit)	Disk	Small cylinder[15]	Parameter analysis
material type	paste		concrete
w/c ratio (-)	0.55	0.485	0.40
Initial capillary porosity ϕ_0 (-)	0.33	0.25	0.11
Porosity in Z_1 zone ϕ_1 (-)	0.402	0.335	0.155
Porosity in Z_2 zone ϕ_2 (-)	0.347	0.248	0.121
Chemical reaction coefficient r_S (m^3/mol)	0.035		
Aluminum hydrates content $n_{C_3AH_6}$ (mol/m^3)	320	520	198
CH content n_{CH} (mol/m^3)	2158	2557	1345
Magnification factor θ (-)	-	4, 5, 6, 7	-
Apparent OH^- diffusivity in Z_1 zone $D_{1,OH}$ (10^{-11} m^2/s)	4.20	1.25, 1.56, 1.87, 2.18	1.23
Apparent OH^- diffusivity in Z_2 zone $D_{2,OH}$ (10^{-12} m^2/s)	6.76	3.12	5.83
Apparent SO_4^{2-} diffusivity in Z_1 zone $D_{1,S}$ (10^{-12} m^2/s)	8.52	1.36, 1.70, 2.04, 2.38	2.50
Apparent SO_4^{2-} diffusivity in Z_2 zone $D_{2,S}$ (10^{-13} m^2/s)	1.12	0.34	1.50
Dissolution equilibrium constant of AFt at 25^{o}C log(AFt) (-)	-44.55[43]		
Dissolution equilibrium constant of C_3AH_6 at 25^{o}C log(C_3AH_6)(-)	-20.49[43]		
Dissolution equilibrium constant of CH at 25^{o}C log(CH) (-)	-5.14[43]		
Molar volume of ettringite V_C (10^{-3} m^3/mol) (-)	0.710[43]		
Biot's coefficient b (-)	0.69[44]		0.54[44]
Tensile strength σ_{ft} (MPa)	2.0[44]		3.1[44]
Measured spalling rate (10^{-4}mm/$s^{0.5}$)	3.19	5.73	-

Not attempting to make parametric analysis for all these quantities, we retain two dimensionless variables related to sulfates, the normalized boundary sulfate concentration c_S^- and the relative apparent sulfate diffusivity D_S^- in crystallized zone, to study their impact on the normalized spalling rate η^-. The simulation results are shown in Figure9, indicating that η^- falls rapidly with the reduction of normalized boundary concentration c_S^- and relative diffusivity D_S^-. Obviously, the lower sulfate concentration on surface boundary and smaller sulfate diffusivity lead to a slower and lower sulfate profile, which in turns gives lower supersaturation degree and effective stress level. Besides, the spalling rate η^- becomes zero as c_S^- and D_S^- become low/small enough. As shown in Figure 8, both the supersaturation degree and effective stress have a local maximum, the zero spalling rate is either due to the maximum $\beta_{AFt} < 1.0$ with no AFt

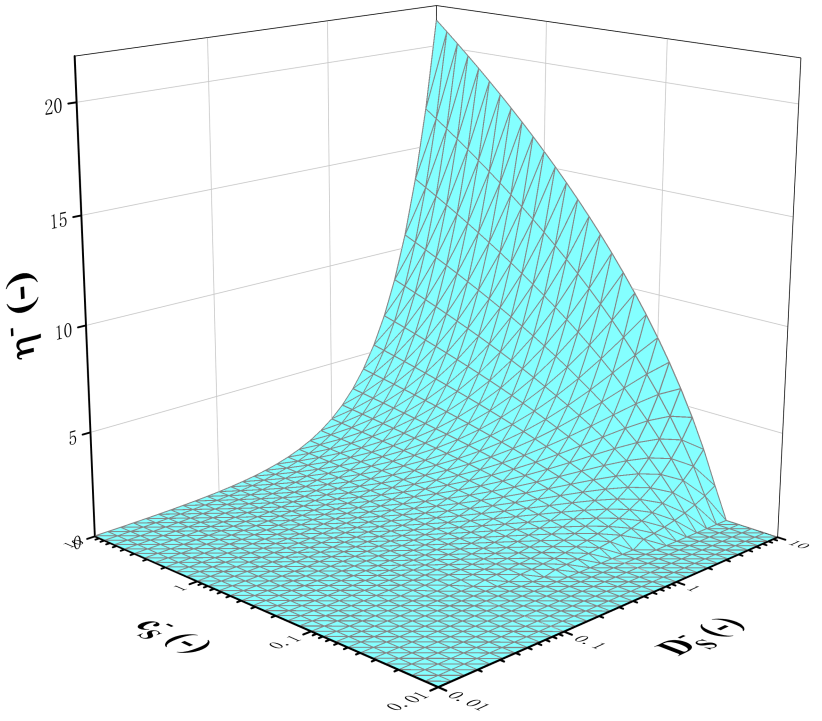

Figure 9: Normalized spalling rate in terms of normalized boundary sulfate concentration and relative sulfate diffusivity. Normalized spalling rate η^- is the ratio of spalling rate η' to the square root of apparent hydroxide diffusivity in dissolved zone $D_{1,\mathrm{OH}}$: $\eta^- = \eta'/2\sqrt{D_{1,\mathrm{OH}}}$. Normalized concentration c_S^- is the ratio of boundary sulfate concentration c_S^0 to the boundary hydroxide concentration c_OH^0: $c_\mathrm{S}^- = c_\mathrm{S}^0/c_\mathrm{OH}^0$. Relative sulfate diffusivity D_S^- is ratio of apparent sulfate diffusivity in crystallized zone $D_{2,\mathrm{S}}$ to the apparent hydroxide diffusivity in dissolved zone $D_{1,\mathrm{OH}}$: $D_\mathrm{S}^- = \sqrt{D_{2,\mathrm{S}}/D_{1,\mathrm{OH}}}$.

formed or due to the maximum $\sigma' < \sigma_{\mathrm{ft}}$.

Four single parameters are selected for parametric analysis to deliver clearer messages for engineering use: the boundary sulfate concentration c_S^0 representing the intensity of environmental sulfates, the apparent sulfate diffusivity in crystallized zone $D_{2,\mathrm{S}}$ depicting the concrete compactness, the aluminium phase content $n_{\mathrm{C_3A}}$ and the portlandite content n_{CH} describing the main chemical characteristics of concrete. The other parameters for a typical concrete material are given in Table 1 and Table B.1. The simulation results are shown in Figure 10. The spalling rate η' increases rapidly with c_S^0 till 30 mol/m^3, then increase with slower rates in Figure 10a. The message for engineering use would be the gradation of environmental action intensity in terms of external sulfate concentration should better be made in logarithm scale. Figure 10b shows η' increases with $D_{2,\mathrm{S}}$: if $D_{2,\mathrm{S}}$ is limited to 10^{-12} m^2/s, the usual value of concrete cover thickness, 50mm, can resist the sulfate spalling for 100 years for the given conditions. Figure 10c presents three stages for spalling rates in terms of C_3A content: $\eta' = 0$ when $n_{\mathrm{C_3A}}$ is in the range of 0-60 mol/m^3; η' quickly rises to around 2.5 mm/a$^{0.5}$ for $n_{\mathrm{C_3A}}$ in the range of 60-100 mol/m^3; slower increase of η' with $n_{\mathrm{C_3A}}$ over 100 mol/m^3. The significant influence of $n_{\mathrm{C_3A}}$ is due to the assumption for sulfate reactions in Eq.(8): bound sulfates n_S are proportional to $n_{\mathrm{C_3A}}$. It is interesting to compare this simulation results with some engineering rules of thumb: for concretes exposed to severe sulfate environments, the C_3A content is normally limited to 5% of the cement contents[45]. For typical concretes with 300-400 kg Portland cement in binders, the limit of C_3A is 15-20 kg, rather near to the simulation result of 60 mol/m^3, i.e. 16.2 kg/m^3 concrete. On the contrary, the results in Figure 10d shows the CH content n_{CH} has little influence on spalling rate until decreasing to about 120 mol/m^3 or 8.88 kg/m^{3}concrete.

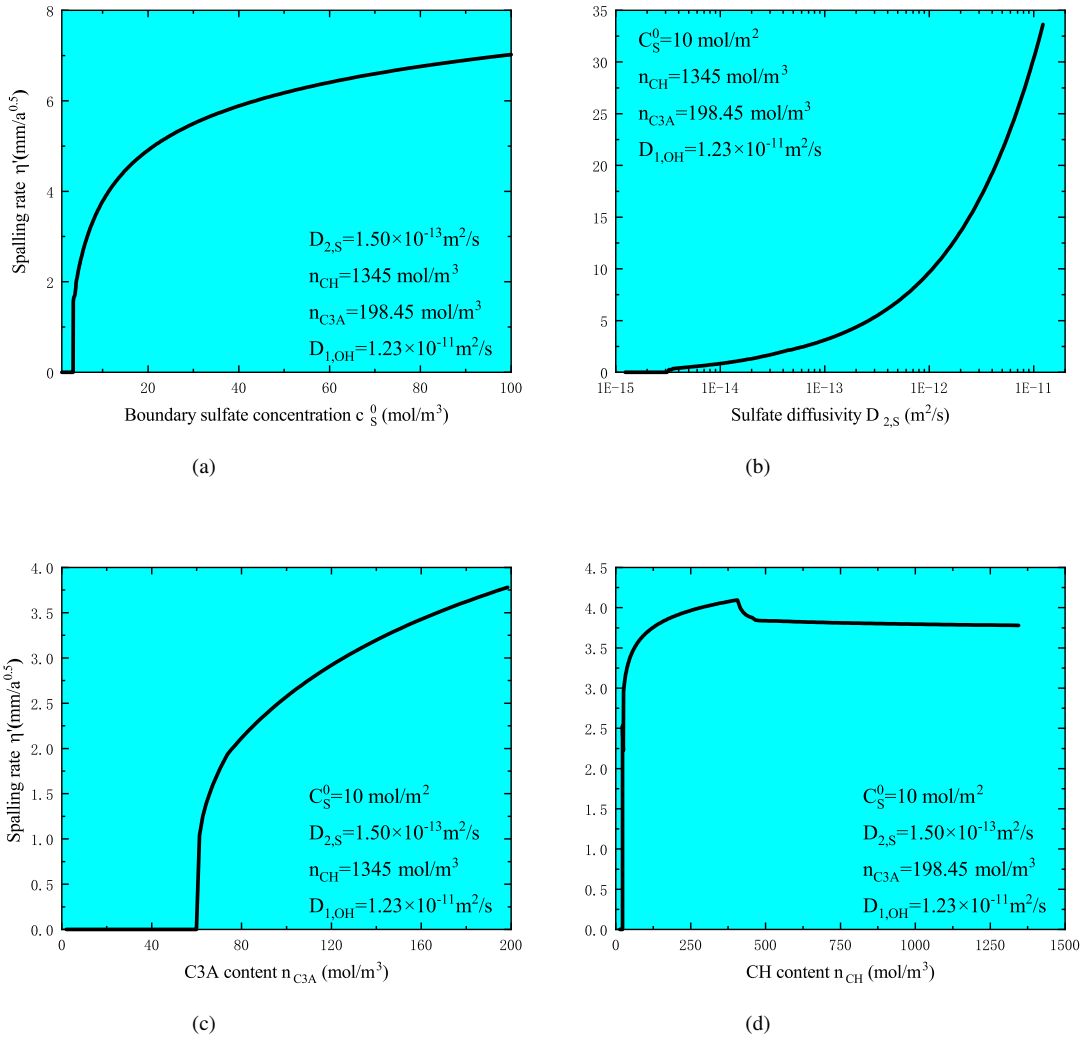

Figure 10: Influence on spalling rate by a)boundary sulfate concentration, b)sulfate diffusivity, c)aluminum phase content, d)portlandite phase content on a concrete material with a w/c of 0.4.

To explore further η' in Figure 10d, we plot the moving rates of three fronts and the A_3 parameter in spalling rate model in terms of n_{CH} in Figure 11. The results in Figure 11a show that higher n_{CH} leads to slower moving rates for crystallization front k and leaching front κ, resulting in smaller A_3 values in Eq.(A.5) in Figure 11b. Figure 11a shows moreover the drop in η' occurs after intersecting with κ curve, indicating the spalling front reaching into intact zone Z_3 in Figure 1. Under this condition, the effective stress takes Eq.$(25)_3$, where the A_3 value is relevant to the effective stress level. Because of the decreasing A_3 value with the CH content n_{CH} in Figure 11b, the effective stress is decreased, leading to the the smaller spalling rate. But again, this occurs only after the spalling font reaching the intact zone Z_3 and this decrease of spalling is less important in magnitude compared to the range $n_{CH} < 400$ mol/m^3 in Figure 10d.

4.2. Critical analysis

In order to obtain simplified and analytical solution for the spalling rates, we inevitably introduced some strong assumptions, including the constant diffusivity in different zones, the leaching of only solid phase of CH, the constant concentration of aluminates in pore solution, and the instantaneous formation of AFt. This section is dedicated to the

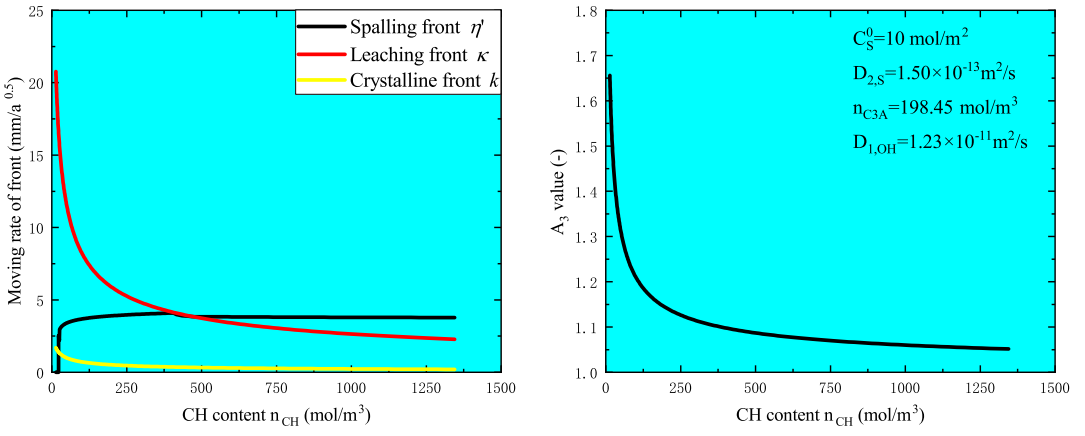

Figure 11: Further analysis of impact of CH content of typical concrete with w/c=0.4: (a) moving rates of the fronts, (b) A_3 value in spalling rate models.

discussion of the advantages and limits of these assumptions so that the valid application scope of spalling rate models can be clarified.

The constant diffusivity comes first. On space scale, constant values of apparent diffusivity are attributed to the three zones: the dissolved zone Z_1, the crystallized zone Z_2 and the intact zone Z_3 in Figure 1, or the cracked zone Z_1, the uncracked zone Z_2 and the intact zone Z_3 in Figure 2. For Z_1 in Figure 1, the AFt and CH are assumed totally dissolved, the pore structure is altered accordingly, and it is rational to assume a constant diffusivity. For Z_1 in Figure 2, the crack openings provide more efficient transport channels for pore species to transport. Considering the relevant experimental results(θ=4-7[41]), it is rational to attribute a different diffusivity from the bulk concrete. But here, the attributed diffusivity remains constant during the spalling process, meaning that the crack openings should be stable otherwise the model in Section 2.4.2 should be reviewed. For Z_2, either the crystallized zone (Figure 1) or uncracked zone (Figure 2), the formation of AFt and the leaching of CH are assumed to cancelled their respective effect, pore filling or enlarging, on pore structure, and the diffusivity of intact concrete is taken. For Z_3 zones, the intact concrete properties are retained due to the very limited AFt formation and no leaching state. Thus, the zone Z_2 and Z_3 merge into one region in terms of the transport properties. On time scale, the diffusivity is also assumed constant. This is challenged by some experimental works[5, 15, 39], which showed the apparent diffusivity decreasing rapidly with exposure time during ESA. It is an alert for the model application: for real engineering cases, one should use long-term diffusivity values instead of the short-term diffusivity values measured in laboratory.

Then come the leaching, the aluminate concentration and AFt formation. As aforementioned, if leaching involves only portlandite, the buffering capacity of CSH, the main cement hydrates, is neglected, leading to the overestimation of leaching rate κ and leaching front X_L. This assumption will be reasonable for concretes using the Portland cement as the main component of binder of which the CH content is important compared to CSH. For binders containing large quantity of supplementary cementitious materials (SCM), this assumption possible gives spalling rates too overestimated to be useful due to the (very) low CH content. Further, the assumption of constant aluminate concentration as its value in intact pore solution, cf. Eq.(17), also overestimates its real value, which should be scaled to the actual concentrations of Ca^{2+} and OH^-. Accordingly, the supersaturation in Eq.(2) is also overestimated, in turn leading to the overestimation of spalling rate. Thus, both assumptions lead to overestimation of spalling rates, i.e. results on conservative side in engineering terms. An improvement may be to include the aluminate ions into the pore transport and establish a new dissolution front for the solid aluminate phases. In our models, the AFt amount is set to be proportional to the sulfate concentration in pore solution, cf. Eq.(8). This has double implications: first, the sulfate reaction is complete and will consume out all the solid aluminate phase; second, the AFt formation is instantaneous without kinetics. So far, there is no unanimity on the kinetics of ettringite crystallization: authors adopted the first-order

or second-order reaction assumption in the literature[21, 46, 47]. But, some experimental results seem to support, at least partially, our assumption: the relative ettringite content measured by the energy dispersive X-ray diffraction (EDXRD) approches the sulfate concentration profile [15]. So, our assumption tends to overestimate the quantity and rate of AFt formation, leading to the overestimation of the supersaturation, effective stress and spalling rate.

To summarize, the assumptions taken in the models, such as leaching of only CH phase, constant aluminate concentration and complete/instantaneous AFt formation, all lead to the overestimation of the effective stress and the spalling rate. In engineering terms, the models provide predictions on conservative side. The constant diffusivity assumption makes trade-off of detailed pore chemistry with simplified and analytical solutions for spalling rates. The model validations in Section 3 confirm the correct magnitude order and the conservative nature of spalling rates predicted by our models, and such models can already help the engineers to choose the appropriate design options. Actually, such models are just expected to provide correct prediction on the order of magnitude of spalling rate, and prudence should be taken as the models are confronted with experimental results. The models should be more reasonably applied to concretes using mainly Portland cement as binder. Moreover, the application of these models should check the actual strain and stress conditions of elements to make the correct choice of damage patterns, especially as external loading and reinforcement are present in structural elements. Last point to be noted is the external sulfate environments: the models apply only as the sulfates dominate in the external aggressive agents; as the other aggressive ions, such as magnesium and chlorides, are present with important concentrations, other damage mechanisms intervene and these models lose their validity.

5. Conclusion

1. A spalling rate model is proposed for concrete exposed to the combined action of ESA and leaching. The pore transport considers the dissolution-diffusion of hydroxide ions and the binding-diffusion of external sulfate ions. The formation of AFt is dictated by the supersaturation degree, the effective stress from pore crystallization is evaluated through poromechanics using the Correns' law, and the fracture criterion is set as the effective tensile stress attaining the tensile strength. The spalling depth is defined as the position where the fracture criterion is satisfied. Two sub-models are developed with respect to two damage patterns: the surface layered spalling and the surface in-plane cracking. For these two cases, the semi-infinite space is divided into three zones: dissolved/cracked zone, crystallized/uncracked zone and the intact zone to leaching. On this basis, the dual moving boundary problems are established and solved for the sulfate and hydroxide profiles. The moving rates for dissolved/cracking front and leaching front are also solved as proportional to the square root of exposure time, so is the spalling depth. Such models incorporate the main knowledge of concrete damage by sulfate chemical reactions and provide analytical results for the damage rate.

2. The established models are validated against two sets of experiments on cement paste specimens exposed to external sulfate solution with pH value of solution controlled to neutral state. The sub-model for layered damage pattern, without cracking effect on diffusivity, is validated against uni-dimensional sulfate diffusion on disk specimens, and the spalling depths measured are used to validate the sub-model. With the consideration of decreased diffusivity by ageing effect, the model gives conservative prediction for spalling rate but on the same order of magnitude as measured one. Then, the sub-model for in-plane cracking is employed to predict the sulfate attack on smaller cylinder specimens. With the help of coordinate transformation, the spalling rate is predicted using the usual range values for cracking magnification for diffusivity, and the model prediction gives conservative results but in good agreement with measured cracking depths. Through the validations, the spalling depth is first confirmed to scale linearly with the square root of exposure time, indicating the the sulfate damage is dominated by diffusion processes. Due to the conservative nature and correct prediction on magnitude order of spalling depth, these models have good potential for engineering use.

3. For the spalling rate model, four groups of parameters interplay: the diffusivities, the boundary ionic concentrations, the contents of reactive solid phases, and the mechanical properties related to fracture. Through dimensionless quantity analysis, the normalized spalling rate drops rapidly as the normalized sulfate concentration and the relative sulfate diffusivity decrease. The single parameter analysis shows that the sulfate diffusivity, in physical aspect, and the aluminate content, in chemical aspect, are two foremost impact factors for spalling damage rate, which provides the basis for technical specification for concretes exposed in such environments. For the intensity classification of combined action of ESA and leaching, the gradation on logarithmic scale of external sulfate concentration is more appropriate. The portlandite content has less important impact on the spalling rate, so the CH content is not relevant to the spalling rate control.

4. Some strong assumptions are made in the modeling for the sake of simplified models and analytical results for spalling depth. Among these assumptions, the leaching of only CH phase, the constant aluminate concentration and complete/instantaneous AFt formation all leads to the overestimation of the effective stress and the spalling rate. The models will be more reasonably applied to concretes using Portland cement as the main component of binder. As long as the prediction is on the correct order of magnitude for spalling depth, the conservative nature of prediction is favored by engineering use. The constant diffusivity assumption on time scale needs attention when the models are applied to real engineering cases, and the long-term diffusivity values should be used instead of laboratory short-term measurements or theoretically estimated value because ageing can occur for diffusivity. Moreover, as other aggressive ions (Mg^{2+}, Cl^{-}) are present along with sulfates in an important concentration, the models should not be used as the damage mechanism would be different from AFt formation.

Acknowledgement

The research is supported by China National Science Foundation Grant No. 52038004. The first author benefits from a mutual doctoral program between Tsinghua university (China) and Université Gustave Eiffel (France).

A. Solution of dual moving boundary problem

The Fick's second law with constant diffusivity can be reduced to an ordinary differential equation using Boltzmann variables [48]. For the dual MBP defined through Eq.(7) to Eq.(11), the following Boltzmann variables are defined.

$$\eta = \frac{x}{\sqrt{t}} \quad \text{and} \quad k = \frac{X_{\mathrm{C}}}{\sqrt{t}},\ \kappa = \frac{X_{\mathrm{L}}}{\sqrt{t}} \tag{A.1}$$

A.1. Sulfate diffusion

The sulfate diffusion equations in Eq.(7) can be rewritten using the Boltzmann variables as

$$-\eta\frac{\partial c_{\mathrm{S}}}{\partial \eta} = \begin{cases} 2D_{1,\mathrm{S}}\dfrac{\partial^2 c_{\mathrm{S}}}{\partial \eta^2}, & \eta < k \\ \\ 2D_{2,\mathrm{S}}\dfrac{\partial^2 c_{\mathrm{S}}}{\partial \eta^2}, & \eta \geq k \end{cases} \tag{A.2}$$

The initial condition, boundary condition and the moving boundary conditions can be also expressed in terms of these Boltzmann variables by putting Eq.(A.1) into Eq.(9),

$$\begin{cases} c_{\mathrm{S}}(\eta \to \infty) = 0, \quad c_{\mathrm{S}}(\eta = 0) = c_{\mathrm{S}}^0 \\ c_{\mathrm{S}}|_{\eta=k^-} = c_{\mathrm{S}}|_{\eta=k^+}, D_{1,\mathrm{S}}\dfrac{\partial c_{\mathrm{S}}}{\partial \eta}\Big|_{\eta=k^-} = D_{2,\mathrm{S}}\dfrac{\partial c_{\mathrm{S}}}{\partial \eta}\Big|_{\eta=k^+} \end{cases} \tag{A.3}$$

It is readily to verify that the following solution satisfies both Eq.(A.2) and Eq.(A.3),

$$\frac{c_{\mathrm{S}}}{c_{\mathrm{S}}^0} = \begin{cases} A_1\mathrm{erfc}\left(\dfrac{\eta}{2\sqrt{D_{1,\mathrm{S}}}}\right) + A_2, & \eta < k \\ \\ A_3\mathrm{erfc}\left(\dfrac{\eta}{2\sqrt{D_{2,\mathrm{S}}}}\right), & \eta \geq k \end{cases} \tag{A.4}$$

And the integral constants $A_{1,2,3,4}$ are expressed as,

$$\begin{cases} A_1 = \dfrac{1}{1 - \mathrm{erfc}\left(\dfrac{K_2}{K_1}\right) + K_1\mathrm{erfc}(K_2)\exp\left(K_2^2 - \dfrac{K_2^2}{K_1^2}\right)} \\ A_2 = 1 - A_1, \quad A_3 = K_1\exp\left(K_2^2 - \dfrac{K_2^2}{K_1^2}\right)A_1 \end{cases} \tag{A.5}$$

with

$$K_1 = \sqrt{\frac{D_{1,\mathrm{S}}}{D_{2,\mathrm{S}}}},\ K_2 = \frac{k}{2\sqrt{D_{2,\mathrm{S}}}} \tag{A.6}$$

A.2. Hydroxide diffusion

The hydroxide diffusion equations in Eq.(10) can be rewritten using the Boltzmann variables as

$$-\eta\frac{\partial c_{\mathrm{OH}}}{\partial \eta} = \begin{cases} 2D_{1,\mathrm{OH}}\dfrac{\partial^2 c_{\mathrm{OH}}}{\partial \eta^2}, & \eta < k \\ 2D_{2,\mathrm{OH}}\dfrac{\partial^2 c_{\mathrm{OH}}}{\partial \eta^2}, & k \le \eta < \kappa \end{cases} \tag{A.7}$$

The initial condition, boundary condition and the moving boundary conditions can be also expressed in terms of these Boltzmann variables by putting Eq.(A.1) into Eq.(11),

$$\begin{cases} c_{\mathrm{OH}}(\eta = 0) = 0,\ \ c_{\mathrm{S}}(\eta \ge \dfrac{X_{\mathrm{L}}}{\sqrt{t}}) = c^0_{\mathrm{OH}} \\ c_{\mathrm{OH}}|_{\eta=k^-} = c_{\mathrm{OH}}|_{\eta=k^+},\ D_{1,\mathrm{OH}}\dfrac{\partial c_{\mathrm{OH}}}{\partial \eta}\Big|_{\eta=k^-} = D_{2,\mathrm{OH}}\dfrac{\partial c_{\mathrm{OH}}}{\partial \eta}\Big|_{\eta=k^+} \end{cases} \tag{A.8}$$

It is readily to verify that the following solution satisfies both Eq.(A.7) and Eq.(A.8),

$$\frac{c_{\mathrm{OH}}}{c^0_{\mathrm{OH}}} = \begin{cases} a_1\mathrm{erf}\left(\dfrac{\eta}{2\sqrt{D_{1,\mathrm{OH}}}}\right), & \eta < k \\ a_2\mathrm{erf}\left(\dfrac{\eta}{2\sqrt{D_{2,\mathrm{OH}}}}\right) + a_3, & k \le \eta < \kappa \\ 1, & \eta \ge \kappa \end{cases} \tag{A.9}$$

And the integral constants $a_{1,2,3,4}$ are expressed as,

$$\begin{cases} a_2 = \dfrac{1}{\mathrm{erf}(\lambda) - \mathrm{erf}\left(\dfrac{k_2}{k_1}\right) + k_1\mathrm{erf}(k_2)\exp\left(k_2^2 - \dfrac{k_2^2}{k_1^2}\right)} \\ a_1 = k_1\exp\left(k_2^2 - \dfrac{k_2^2}{k_1^2}\right)a_2, \quad a_3 = 1 - \mathrm{erf}(\lambda)a_2 \end{cases} \tag{A.10}$$

with

$$k_1 = \sqrt{\frac{D_{2,\mathrm{OH}}}{D_{1,\mathrm{OH}}}},\ k_2 = \frac{k}{2\sqrt{D_{1,\mathrm{OH}}}};\quad \lambda = \frac{\kappa}{2\sqrt{D_{2,\mathrm{OH}}}} \tag{A.11}$$

B. Transport properties

A multi-scale model is adopted to estimate the ionic diffusivity for SO_4^{2-} and OH^- in this study [38]. Following this scheme, the ionic diffusivity is expressed as

$$D_i^e = \frac{1 - \lambda_{\mathrm{ca}}\upsilon_{\mathrm{ca}}}{1 - \lambda_{\mathrm{fa}}\upsilon_{\mathrm{fa}}}\upsilon_{\mathrm{paste}}f(\phi_{\mathrm{p}})D_0^i \tag{B.1}$$

where D_i^e is the effective diffusivity of ion species i in the concrete pore solution, $\lambda_{\mathrm{ca,fa}}$ are the tortuosity parameters for the coarse and fine aggregates, $v_{\mathrm{ca,fa}}$ are the volumetric fractions of coarse and fine aggregates in concrete, $f(\phi_{\mathrm{p}})$ is the percolation function for ionic diffusion through pores, ϕ_{p} is the capillary porosity of cement paste in concrete, and D_i^0 is the diffusivity of ion i in pure water. The percolation function takes the following form[49],

$$f(\phi_{\mathrm{p}}) = 0.001 + 0.07\phi_{\mathrm{p}}^2 + 1.8 < \phi_{\mathrm{p}} - 0.18 > (\phi_{\mathrm{p}} - 0.18)^2 \tag{B.2}$$

with $< x >= x$ when $x \geq 0$ and $< x >= 0$ when $x < 0$. Without binding between the ions and the solid matrix, the apparent diffusivity writes,

$$D_i^a = \frac{D_i^e}{\phi} \tag{B.3}$$

For sulfate ions, there exists chemical binding between the ions and the solid matrix. The apparent sulfate diffusivity in crystallized zone $D_{2,\mathrm{S}}$ takes into account the chemical binding by AFt formation through,

$$D_{2,\mathrm{S}} = \frac{D_{2,\mathrm{S}}^i}{\phi_2(1 + r_{\mathrm{S}} n_{\mathrm{C_3A}})} \tag{B.4}$$

The parameters and the apparent diffusivities in the dissolved and crystallized zones are provided in TableB.1 for different usages.

C. Diffusion in 1D axis-symmetry case

In 1D axis-symmetry case, the Fick's second law with constant diffusivity is converted into radical coordinate system as,

Table B.1
Parameters and values for apparent diffusvity of SO_4^{2-} and OH^- ions

Parameter(unit)	Disk	Small cylinder[15]	Parameter analysis
Initial capillary porosity ϕ_0 (-)	0.33	0.25	0.11
Porosity change $\Delta\phi_1$ (-) by leaching	0.072	0.085	0.045
Porosity change $\Delta\phi_2$ (-) by sulfate attack	0.055	0.087	0.034
Porosity in dissolved zone ϕ_1 (-)	-0.402	-0.335	-0.155
Porosity in crystallized zone ϕ_2 (-)	0.347	0.248	0.121
Pore percolation function in Z_1 zone $f(\phi_1)$ (-)	0.0320	0.0155	0.0474
Pore percolation function in Z_2 zone $f(\phi_2)$ (-)	0.0178	0.0059	0.0175
Fine aggregate content v_{fa} (-)	0	0	0.26
Coarse aggregate content v_{ca} (-)	0	0	0.39
Cement paste content v_{paste} (-)	1	1	0.35
OH^- diffusivity in water D_{OH}^0 (10^{-9} m^2/s)	5.27		
SO_4^{2-} diffusivity in water D_{S}^0 (10^{-9} m^2/s)	1.07		
Effective OH^- diffusivity in Z_1 zone $D_{1,\mathrm{OH}}^e$ (10^{-12} m^2/s)	16.86	8.20	1.91
Effective OH^- diffusivity in Z_2 zone $D_{2,\mathrm{OH}}^e$ (10^{-12} m^2/s)	9.39	3.09	0.71
Effective SO_4^{2-} diffusivity in Z_1 zone $D_{1,\mathrm{S}}^e$ (10^{-12} m^2/s)	3.42	1.67	0.39
Effective SO_4^{2-} diffusivity in Z_2 zone $D_{2,\mathrm{S}}^e$ (10^{-12} m^2/s)	1.91	0.63	0.14
Apparent OH^- diffusivity in Z_1 zone $D_{1,\mathrm{OH}}$ (10^{-11} m^2/s)	4.20	2.45	1.23
Apparent OH^- diffusivity in Z_2 zone $D_{2,\mathrm{OH}}$ (10^{-11} m^2/s)	2.71	1.25	0.58
Apparent SO_4^{2-} diffusivity in Z_1 zone $D_{1,\mathrm{S}}$ (10^{-12} m^2/s)	8.52	4.97	2.50
Chemical reaction coefficient r (m^3/mol)	0.035		
Aluminum phase content $n_{\mathrm{C_3A}}$ (mol/m^3)	320	520	198
Apparent SO_4^{2-} diffusivity in Z_2 zone $D_{2,\mathrm{S}}$ (10^{-13} m^2/s)	4.50	1.35	1.49

$$\frac{\partial c}{\partial t} = D(\frac{1}{r}\frac{\partial c}{\partial r} + \frac{\partial^2 c}{\partial r^2}) \tag{C.1}$$

Accordingly, the sulfate and hydroxide diffusion equations with a moving boundary R_M and leaching front R_L write,

$$\begin{cases} \frac{\partial c_S}{\partial t} = D_{1,S}(\frac{c_S}{r} + r\frac{\partial^2 c_S}{\partial r^2}), & \frac{\partial c_{OH}}{\partial t} = D_{1,OH}(\frac{c_{OH}}{r} + r\frac{\partial^2 c_{OH}}{\partial r^2}), & R_M \le r \le R \\ \frac{\partial c_S}{\partial t} = D_{2,S}(\frac{c_S}{r} + r\frac{\partial^2 c_S}{\partial r^2}), & \frac{\partial c_{OH}}{\partial t} = D_{2,OH}(\frac{c_{OH}}{r} + r\frac{\partial^2 c_{OH}}{\partial r^2}), & R_L \le r < R_M \\ \frac{\partial c_S}{\partial t} = D_{2,S}(\frac{c_S}{r} + r\frac{\partial^2 c_S}{\partial r^2}), & \frac{\partial c_{OH}}{\partial t} = 0, & 0 \le r < R_L \end{cases} \tag{C.2}$$

where R represents the radius of cylinder specimen. For sulfate diffusion, the initial condition and boundary conditions, at the surface boundary and moving boundary in Eq.(9), write,

$$\begin{cases} c_S(r < R, t = 0) = 0,\ c_S(r = R, t > 0) = c_S^0 \\ c_S|_{r=R_M^-} = c_S|_{r=R_M^+},\ rD_{1,S}\frac{\partial c_S}{\partial r}\Big|_{r=R_M^-} = rD_{2,S}\frac{\partial c_S}{\partial r}\Big|_{r=R_M^+} \end{cases} \tag{C.3}$$

For hydroxide diffusion, the initial condition and boundary conditions, at the surface and moving boundaries in Eq.(11), write,

$$\begin{cases} c_{OH}(r = 0, t > 0) = 0, \quad c_{OH}(r \le R_L) = c_{OH}^0 \\ c_{OH}|_{r=R_M^-} = c_{OH}|_{r=R_M^+}, \quad rD_{1,OH}\frac{\partial c_{OH}}{\partial r}\Big|_{r=R_M^-} = rD_{2,OH}\frac{\partial c_{OH}}{\partial x}\Big|_{r=R_M^+} \\ n_{CH}\frac{\mathrm{d}R_L}{\mathrm{d}t} = -\phi_2 D_{2,OH}\frac{\partial c_{OH}}{\partial r}\Big|_{r=R_L} \end{cases} \tag{C.4}$$

References

[1] O. S. B. Al-Amoudi, Sulfate attack and reinforcement corrosion in plain and blended cements exposed to sulfate environments, Building and Environment 33 (1998) 53–61. doi:https://doi.org/10.1016/S0360-1323(97)00022-X.

[2] B. Tian, M. D. Cohen, Does gypsum formation during sulfate attack on concrete lead to expansion?, Cement and Concrete Research 30 (2000) 117–123. doi:https://doi.org/10.1016/S0008-8846(99)00211-2.

[3] M. Santhanam, M. D. Cohen, J. Olek, Effects of gypsum formation on the performance of cement mortars during external sulfate attack, Cement and Concrete Research 33 (2003) 325–332. doi:https://doi.org/10.1016/S0008-8846(02)00955-9.

[4] T. Ikumi, S. H. Cavalaro, I. Segura, A. de la Fuente, A. Aguado, Simplified methodology to evaluate the external sulfate attack in concrete structures, Materials Design 89 (2016) 1147–1160. doi:https://doi.org/10.1016/j.matdes.2015.10.084.

[5] R. Ragoug, O. O. Metalssi, F. Barberon, J.-M. Torrenti, N. Roussel, L. Divet, J.-B. d'Espinose de Lacaillerie, Durability of cement pastes exposed to external sulfate attack and leaching: Physical and chemical aspects, Cement and Concrete Research 116 (2019) 134–145. doi:https://doi.org/10.1016/j.cemconres.2018.11.006.

[6] L. Irbe, R. Beddoe, D. Heinz, The role of aluminium in c-a-s-h during sulfate attack on concrete, Cement and Concrete Research 116 (2019) 71–80. doi:https://doi.org/10.1016/j.cemconres.2018.11.012.

[7] Y. Gu, R.-P. Martin, O. Omikrine Metalssi, T. Fen-Chong, P. Dangla, Pore size analyses of cement paste exposed to external sulfate attack and delayed ettringite formation, Cement and Concrete Research 123 (2019) 105766. doi:https://doi.org/10.1016/j.cemconres.2019.05.011.

[8] Z. Zhang, J. Zhou, J. Yang, Y. Zou, Z. Wang, Understanding of the deterioration characteristic of concrete exposed to external sulfate attack: Insight into mesoscopic pore structures, Construction and Building Materials 260 (2020) 119932. doi:https://doi.org/10.1016/j.conbuildmat.2020.119932.

[9] T. Ikumi, I. Segura, S. H. Cavalaro, Effects of biaxial confinement in mortars exposed to external sulfate attack, Cement and Concrete Composites 95 (2019) 111–127. doi:https://doi.org/10.1016/j.cemconcomp.2018.10.017.

[10] J. Haufe, A. Vollpracht, Tensile strength of concrete exposed to sulfate attack, Cement and Concrete Research 116 (2019) 81–88. doi:https://doi.org/10.1016/j.cemconres.2018.11.005.

[11] P. W. Brown, An evaluation of the sulfate resistance of cements in a controlled environment, Cement and Concrete Research 11 (1981) 719–727. doi:https://doi.org/10.1016/0008-8846(81)90030-2.

[12] C. Xiong, L. Jiang, Y. Xu, H. Chu, M. Jin, Y. Zhang, Deterioration of pastes exposed to leaching, external sulfate attack and the dual actions, Construction and Building Materials 116 (2016) 52–62. doi:https://doi.org/10.1016/j.conbuildmat.2016.04.133.

[13] D. Bonen, M. D. Cohen, Magnesium sulfate attack on portland cement paste — ii. chemical and mineralogical analyses, Cement and Concrete Research 22 (1992) 707–718. doi:https://doi.org/10.1016/0008-8846(92)90023-O.

[14] H. Haynes, Sulfate attack on concrete: Laboratory vs. field experience, Concrete International 22 (2002) 64–70.

[15] N. N. Naik, Sulfate attack on Portland cement-based materials: mechanisms of damage and long-term performance, Georgia Institute of Technology, 2003.

[16] C. Carde, R. François, Modelling the loss of strength and porosity increase due to the leaching of cement pastes, Cement and Concrete Composites 21 (1999) 181–188. doi:https://doi.org/10.1016/S0958-9465(98)00046-8.

[17] M. Jebli, F. Jamin, E. Garcia-Diaz, M. El Omari, M. El Youssoufi, Influence of leaching on the local mechanical properties of an aggregate-cement paste composite, Cement and Concrete Composites 73 (2016) 241–250. doi:https://doi.org/10.1016/j.cemconcomp.2016.05.001.

[18] Y. S. Choi, E. I. Yang, Effect of calcium leaching on the pore structure, strength, and chloride penetration resistance in concrete specimens, Nuclear Engineering and Design 259 (2013) 126–136. doi:https://doi.org/10.1016/j.nucengdes.2013.02.049.

[19] K. Kurumisawa, K. Haga, D. Hayashi, H. Owada, Effects of calcium leaching on diffusion properties of hardened and altered cement pastes, Physics and Chemistry of the Earth, Parts A/B/C 99 (2017) 175–183. doi:https://doi.org/10.1016/j.pce.2017.03.007, mechanisms and Modelling of Waste-Cement and Cement-Host Rock Interactions.

[20] B. Bary, Simplified coupled chemo-mechanical modeling of cement pastes behavior subjected to combined leaching and external sulfate attack, International journal for numerical and analytical methods in geomechanics 32 (2008) 1791–1816. doi:https://doi.org/10.1002/nag.696.

[21] B. Bary, N. Leterrier, E. Deville, P. Le Bescop, Coupled chemo-transport-mechanical modelling and numerical simulation of external sulfate attack in mortar, Cement and Concrete Composites 49 (2014) 70–83. doi:https://doi.org/10.1016/j.cemconcomp.2013.12.010.

[22] N. Cefis, C. Comi, Chemo-mechanical modelling of the external sulfate attack in concrete, Cement and Concrete Research 93 (2017) 57–70. doi:https://doi.org/10.1016/j.cemconres.2016.12.003.

[23] S. Qin, D. Zou, T. Liu, A. Jivkov, A chemo-transport-damage model for concrete under external sulfate attack, Cement and Concrete Research 132 (2020) 106048. doi:https://doi.org/10.1016/j.cemconres.2020.106048.

[24] J. Marchand, I. Odler, J. P. Skalny, Sulfate attack on concrete, CRC Press, 2001.

[25] J.-M. Tulliani, L. Montanaro, A. Negro, M. Collepardi, Sulfate attack of concrete building foundations induced by sewage waters, Cement and Concrete Research 32 (2002) 843–849. doi:https://doi.org/10.1016/S0008-8846(01)00752-9.

[26] M. Lei, L. Peng, C. Shi, S. Wang, Experimental study on the damage mechanism of tunnel structure suffering from sulfate attack, Tunnelling and Underground Space Technology 36 (2013) 5–13. doi:https://doi.org/10.1016/j.tust.2013.01.007.

[27] A. Atkinson, J. A. Hearne, Mechanistic model for the durability of concrete barriers exposed to sulphate-bearing groundwaters, MRS Online Proceedings Library (OPL) 176 (1989). doi:https://doi.org/10.1557/PROC-176-149.

[28] D. Damidot, F. Glasser, Thermodynamic investigation of the caoal2o3caso4h2o system at 25°c and the influence of na2o, Cement and Concrete Research 23 (1993) 221–238. doi:https://doi.org/10.1016/0008-8846(93)90153-Z.

[29] N. Naik, A. Jupe, S. Stock, A. Wilkinson, P. Lee, K. Kurtis, Sulfate attack monitored by microct and edxrd: Influence of cement type, water-to-cement ratio, and aggregate, Cement and Concrete Research 36 (2006) 144–159. doi:https://doi.org/10.1016/j.cemconres.2005.06.004.

[30] M. Mainguy, O. Coussy, Propagation fronts during calcium leaching and chloride penetration, Journal of Engineering Mechanics 126 (2000) 250–257. doi:https://doi.org/10.1061/(ASCE)0733-9399(2000)126:3(250).

[31] K. Li, Durability design of concrete structures: Phenomena, modeling, and practice, John Wiley & Sons, 2016.

[32] B. Gebhart, Heat Conduction and Mass Diffusion, New York: McGraw-Hill, 1993.

[33] K. Li, F. Zhao, Y. Zhang, Influence of carbonation on the chloride ingress into concrete: Theoretical analysis and application to durability design, Cement and Concrete Research 123 (2019) 105788. doi:https://doi.org/10.1016/j.cemconres.2019.105788.

[34] M. Xie, P. Dangla, K. Li, Reactive transport modelling of concurrent chloride ingress and carbonation in concrete, Materials and Structures 54 (2021) 1–19. doi:https://doi.org/10.1617/s11527-021-01769-9.

[35] C. W. Correns, Growth and dissolution of crystals under linear pressure, Discussions of the Faraday society 5 (1949) 267–271.

[36] O. Coussy, Mechanics and physics of porous solids, John Wiley & Sons, 2011.

[37] Y. Gu, P. Dangla, R.-P. Martin, O. Omikrine Metalssi, T. Fen-Chong, Modeling the sulfate attack induced expansion of cementitious materials based on interface-controlled crystal growth mechanisms, Cement and Concrete Research 152 (2022) 106676. doi:https://doi.org/10.1016/j.cemconres.2021.106676.

[38] K. Yokozeki, K. Watanabe, N. Sakata, N. Otsuki, Modeling of leaching from cementitious materials used in underground environment, Applied clay science 26 (2004) 293–308. doi:https://doi.org/10.1016/j.clay.2003.12.027.

[39] P. J. Tumidajski, G. Chan, K. E. Philipose, An effective diffusivity for sulfate transport into concrete, Cement and Concrete Research 25 (1995) 1159–1163. doi:https://doi.org/10.1016/0008-8846(95)00108-O.

[40] P. Dangla, A modeling platform based on finite volume/element method, 2022. URL: https://github.com/ifsttar/bil.

[41] B. Gérard, J. Marchand, Influence of cracking on the diffusion properties of cement-based materials: Part i: Influence of continuous cracks on the steady-state regime, Cement and Concrete Research 30 (2000) 37–43. doi:https://doi.org/10.1016/S0008-8846(99)00201-X.

[42] E. Buckingham, On physically similar systems; illustrations of the use of dimensional equations, Physical review 4 (1914) 345.

[43] A. Grandclerc, P. Dangla, M. Gueguen-Minerbe, T. Chaussadent, Modelling of the sulfuric acid attack on different types of cementitious materials, Cement and Concrete Research 105 (2018) 126–133. doi:https://doi.org/10.1016/j.cemconres.2018.01.014.

[44] F.-J. Ulm, G. Constantinides, F. H. Heukamp, Is concrete a poromechanics materials?—a multiscale investigation of poroelastic properties, Materials and structures 37 (2004) 43–58. doi:https://doi.org/10.1007/BF02481626.

[45] ASTM C150/C150M, Standard Specification for Portland Cement, ASTM International, West Conshohocken, US, 2016.
[46] R. Tixier, B. Mobasher, Modeling of damage in cement-based materials subjected to external sulfate attack. i: Formulation, Journal of Materials in Civil Engineering 15 (2003) 305–313. doi:https://doi.org/10.1061/(ASCE)0899-1561(2003)15:4(305).
[47] T. Ikumi, S. H. Cavalaro, I. Segura, A. Aguado, Alternative methodology to consider damage and expansions in external sulfate attack modeling, Cement and Concrete Research 63 (2014) 105–116. doi:https://doi.org/10.1016/j.cemconres.2014.05.011.
[48] J. Crank, The mathematics of diffusion, Oxford university press, 1979.
[49] E. Garboczi, D. Bentz, Computer simulation of the diffusivity of cement-based materials, Journal of materials science 27 (1992) 2083–2092. doi:https://doi.org/10.1007/BF01117921.